ACS APPLIED MATERIALS & INTERFACES

Research Article

www.acsami.org

Comparative Study of Vapor- and Solution-Crystallized Perovskite for Planar Heterojunction Solar Cells

Tian Du,[†,§] Ning Wang,*[,†] Haijun Chen,[†] Hong Lin,[‡] and Hongcai He[†]

[†]State Key Laboratory of Electronic Thin Films and Integrated Devices, University of Electronic Science and Technology of China, Chengdu 610054, P.R. China

[‡]Department of Materials Science and Engineering, Tsinghua University, Beijing 100084, P.R. China

[§]Department of Materials, Imperial College London, London, SW7 2AZ, United Kingdom

ABSTRACT: Organometal halide perovskite ($CH_3NH_3PbI_3$) could be crystallized by exposing PbI_2 to either CH_3NH_3I solution or CH_3NH_3I vapor. Though high performance was achieved in both approaches, it was still not clear which approach would be more desirable for device performance in principle. Herein, we addressed this issue by investigating the influence of crystallization condition on perovskite morphology, and subsequently on device performances. We found that vapor-crystallized perovskite devices demonstrated smoother surface morphology, better light absorption, lower charge recombination, and thus much higher conversion efficiency than solution-crystallized devices, which would give some useful enlightenment to develop high-performance planar perovskite solar cells.

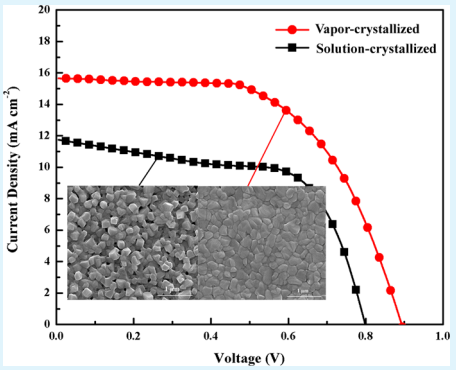

KEYWORDS: *solar cells, photovoltaic performance, perovskite, organometal halide, crystallization*

1. INTRODUCTION

Since the discovery of organometal halide perovskite ($CH_3NH_3PbX_3$, X = Cl, Br, I) as an excellent light harvester for photovoltaic devices,[1−5] in recent years, great achievements in developing high-efficiency, low-cost perovskite-based solar cells have been made.[6−9] The power conversion efficiency of perovskite-based solar cells increased from 3 to 4% at early stage to over 15% at present.[10,11] There are mainly two types of architectures for perovskite-based solar cells. The first one inherited the structure of dye-sensitized solar cells, which was featured with a mesoporous layer of semiconductor nanoparticles, such as TiO_2,[8,12,13] as a scaffold to support perovskite. However, researchers discovered that equally high performance was also achieved after replacing the semiconducting TiO_2 with insulating Al_2O_3.[14,15] Another planar architecture was presented where no mesoporous layer existed and perovskite was deposited directly on planar blocking layer.[16] Planar-structured solar cells showed the advantage of more simplified device architecture and lower processing cost. Intense researches were conducted to fabricate high-efficiency perovskite-based solar cells with planar structure.[17−21]

As for the fabrication of planar-structured perovskite-based solar cells, the perovskite layer was previously deposited on plane blocking layer through one-step method, by spin-coating solution that contained a mixture of organic CH_3NH_3X (X = I, Br, Cl) and inorganic PbX_2 (X = Cl, I) precursor.[22−24] However, a major problem for this method was that the coverage of perovskite was not high and obvious pinholes remained,[25] so that hole transportation layer might directly contact with blocking layer and electrical shorting would happen. High coverage of perovskite could be achieved by an alternative two-step method. In this method, PbI_2 was first deposited on compact TiO_2 by spin-coating, and then PbI_2-coated substrates were dipped into CH_3NH_3I solution to crystallize perovskite.[19,26−28] Though highly efficient devices could be prepared in this dipping approach, there was still a shortcoming that the surface morphology was relatively rough because of the drastic reaction when dipping PbI_2-coated substrates into CH_3NH_3I solution. Another moderate approach was demonstrated by changing the environment of perovskite crystallization. Instead of dipping PbI_2 into CH_3NH_3I solution, the PbI_2-coated substrates were exposed to CH_3NH_3I vapor to crystallize perovskite in a much slower way. This approach was reported to be capable of improving the quality of perovskite to enhance the efficiency of devices.[29] Later, a novel simple and moderate method of sequential vapor-phase deposition was proposed with maximum PEC up to 15.4%.[30,31]

So far, both approaches yielded high-efficiency devices because of their state-of-the-art fabrication techniques. But the question remained that which approach could be more favorable in fabricating a high-efficiency device in general level, or how the crystallization condition could influence the electrical and optical properties of the solar cells. Herein, we systematically characterized the devices fabricated using these

Received: December 2, 2014
Accepted: January 15, 2015
Published: January 15, 2015

DOI: 10.1021/am508495r
ACS Appl. Mater. Interfaces 2015, 7, 3382−3388

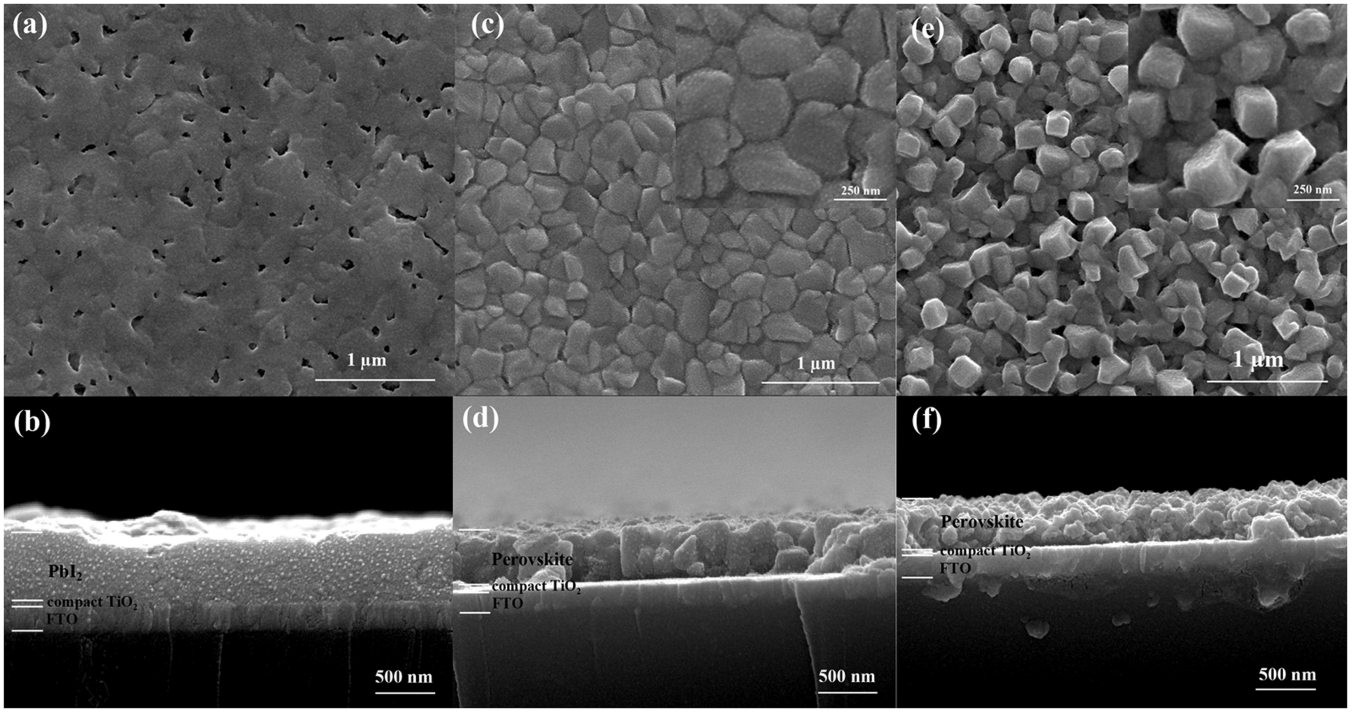

Figure 1. Top-view scanning electron microscopy (SEM) images of (a) PbI_2, (c) vapor-crystallized perovskite, and (e) solution-crystallized perovskite; the insets of c and e show magnified images of perovskite crystals. (b, d, f) Corresponding cross-view SEM images of PbI_2, vapor-crystallized perovskite, and solution-crystallized perovskite.

two approaches. Vapor-crystallized perovskite solar cell demonstrated optimized surface morphology, as well as better electrical and optical properties than solution-crystallized perovskite solar cell. Subsequently, the power conversion efficiency (PEC) for vapor-crystallized device, 8.1%, was much higher than that of solution-crystallized device, 5.8%.

2. EXPERIMENTAL SECTION

Materials. CH_3NH_3I was synthesized by the method reported in ref 2. Briefly, 30 mL of methylamine (40% in methanol) was mixed with 32.3 mL of hydroiodic acid (57 wt % in water) in a round-bottom flask at 0 °C for 2 h with stirring. The solvent was removed by heating the solution in a rotary evaporator at 50 °C for 30 min. The white-yellow precipitate of raw CH_3NH_3I was washed by ethanol, filtered and then washed by diethyl ether again. This procedure was repeated three times. After the last filtration, the products were dried at 70 °C in a vacuum oven overnight.

Device Fabrication. Fluorine-doped tin oxide (FTO) glass (15 Ω/□) was first etched off a strip of conductive area on the edge side by HCl and Zn powders. The etched substrates were then sequentially cleaned in soap water, acetone, deionized water, and ethanol in ultrasonic bath, and were dried under argon flow. A compact TiO_2 (c-TiO_2) blocking layer was prepared by spin-coating tetrabutyl titanate (20 mM in isopropanol) at 2000 rpm for 10 s, followed by annealing at 500 °C for 30 min in air.

PbI_2 was deposited on c-TiO_2 by spin coating a DMF solution of PbI_2 (1.2 M) at 3000 rpm for 15 s. The PbI_2 film was then annealed at 80 °C a the hot plate to remove the remaining solvent. Subsequently, we fixed PbI_2-coated substrates about 5 mm above evenly sprayed CH_3NH_3I powders, with PbI_2-coated side facing downward. The powders were heated at 155 °C for 60 min on the hot plate. The color of the thin film changed gradually from yellow to dark brown. After cooling to room temperature, the perovskite was washed by isopropanol and dried on the hot plate at 80 °C for 5 min. As a comparison, solution-processing method was also used to prepare planar perovskite solar cells. We dipped the PbI_2 film into CH_3NH_3I solution (10 mg mL^{-1} in isopropanol) for 2 min. The color of the film changed from yellow to dark brown immediately after dipping. The devices were then washed by isopropanol and dried on the hot plate at 80 °C.

For devices prepared in both methods, hole-transportation layers were deposited by spin coating spiro-OMeTAD solution (80 mg spiro-OMeTAD (Ningbo Borun), 28.5 mL of 4-*tert*-butylpyridine and 17.5 mL of lithium-bis(trifluoromethanesulfonyl)imide (Li-TFSI) solution (520 mg of Li-TFSI in 1 mL of acetonitrile) all dissolved in 1 mL of chlorobenzene) at 3000 rpm for 45 s. Finally, 120 nm Ag back contact was thermally evaporated on hole-transportation layer under ~1×10^{-6} Torr vacuum condition. The perovskite layer and hole-transportation layer were fabricated in an argon-filled glovebox, with H_2O content below 10 ppm.

Device Characterization. Scanning electron microscopy (SEM) images were taken by JSM-7500F SEM (JEOL, Japan). The measurement was conducted under 20 kV. Atomic force microscopy (AFM) images were taken by SPI3800N (NSK, Japan) under tapping mode. The images and surface roughness data were given by SPIWin software. X-ray diffraction was measured by X'Pert Pro MPD (Phillips, The Netherlands) from 10° to 60°, with a scanning speed of 5° per minute. Ultraviolet−visible absorbance spectra were measured by UV2100 (Shimadzu, Japan) from 380 to 900 nm. Electronic impedance spectroscopy (EIS) was measured at the CHI-660 electrochemical workstation, the data were fitted using ZView software to obtain Nyquist plot.

The photovoltaic performance was measured by Keithley 2400 source meter under AM 1.5 irradiation generated by a solar simulator (XES 301S, SAN-EI Electric Co., LTD). The intensity of irradiation was calibrated by a Si reference cell. *J*−*V* curves were measured by scanning from open circuit (forward bias) to short circuit.

3. RESULTS AND DISCUSSION

Figure 1a, c and e showed the typical top-view scanning electron microscopy (SEM) images of PbI_2, vapor-crystallized perovskite and solution-crystallized perovskite. Figure 1b, d, and f showed the corresponding cross-view SEM images. In Figure 1a, PbI_2 smoothly covered almost the entire area of

DOI: 10.1021/am508495r
ACS Appl. Mater. Interfaces 2015, 7, 3382−3388

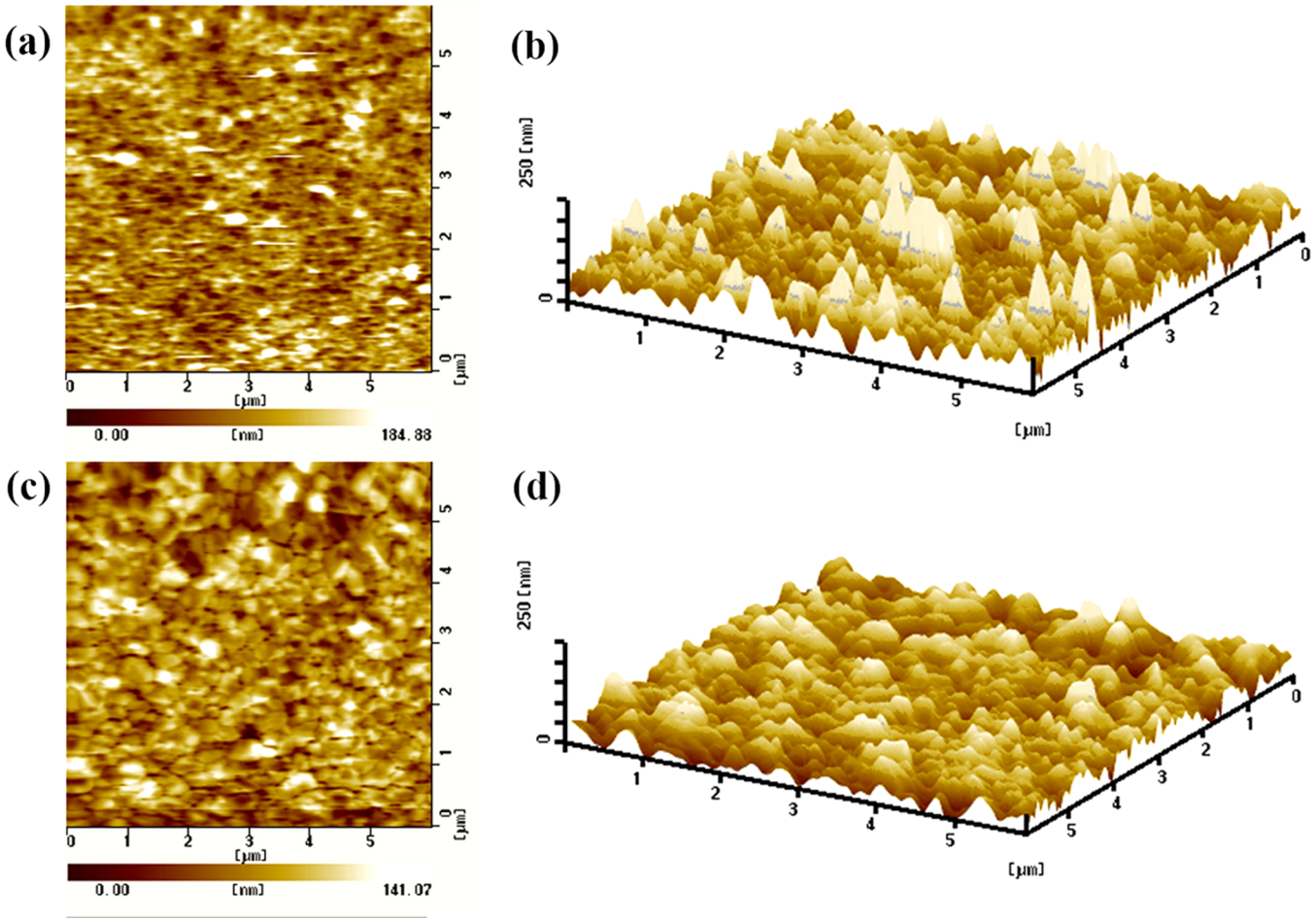

Figure 2. Two-dimension atomic force microscopy (AFM) images of (a) solution-crystallized perovskite and (c) vapor-crystallized perovskite; (b, d) corresponding three-dimension graphs of solution-crystallized perovskite and vapor-crystallized perovskite.

compact TiO_2 with only a few voids. A remarkable difference in surface morphology of perovskite could be observed in Figure 1c, e. Solution-crystallized perovskite consisted of loosely accumulated cubic crystals (Figure 1e), with obvious voids and pinholes. This could be attributed to the drastic chemical reaction when dipping PbI_2-coated substrates into CH_3NH_3I solution, where the yellow color changed into dark brown immediately after dipping. The crystallization process of $CH_3NH_3PbI_3$ perovskite featured the insertion of CH_3NH_3I into layered PbI_2 crystals.[32] Drastic crystallization of perovskite might break the layered structure of PbI_2 and distorted the smooth morphology, resulted in perovskite crystals with disordered alignment. However, the vapor-crystallization method was featured with a much more moderate chemical reaction, and the color changed slowly from yellow to dark brown. Thus, the morphology of PbI_2 thin film was retained and we could see compactly aligned perovskite with smooth surface (Figure 1c). In cross-view SEM images, solution-crystallized perovskite showed small crystals, whereas the vapor-crystallized perovskite demonstrated larger columnar crystals in vertical orientation. For planar-structured solar cells, electrons must diffuse through the whole perovskite layer, and thus vertically oriented crystals were desirable for electron transportation.

To quantitatively characterize the surface roughness of perovskite layer prepared in both methods, atomic force microscopy (AFM) was employed under tapping mode. Figure 2a, c shows comparative two-dimension AFM images of the two categories of perovskite layers in 6 μm × 6 μm area. Figure 2b, d shows corresponding three-dimension plots. As for vapor-crystallized perovskite, the root-mean-square (RMS) of surface roughness was 21.4 nm, much lower than 29.4 nm for solution-crystallized perovskite, which indicated the surface of vapor-crystallized perovskite was smoother than solution-crystallized perovskite.

X-ray diffraction (XRD) was employed to investigate the formation $CH_3NH_3PbI_3$ through both solution and vapor methods. Because the c-TiO_2 blocking layer presents a smooth surface, we thus prepared $CH_3NH_3PbI_3$ on noncrystal glass and the patterns are shown in Figure 3. According to the literature, spin-coated PbI_2 from DMF solution at room temperature demonstrated 2H polytype, with the most intense (001) diffraction peak at 12.65°.[32] $CH_3NH_3PbI_3$ showed characteristic peak of (110) at 14.08°.[33] In solution-crystallized method, the conversion of PbI_2 to $CH_3NH_3PbI_3$ was incomplete after 2 min of dipping, with (001) peak of PbI_2 still remaining. We speculated that CH_3NH_3I in solution could hardly penetrate into PbI_2 thin film and some PbI_2 that was away from the surface stayed unreacted. The agrees with previous findings that (001) peak of PbI_2 appeared remained even after 45 min and 4 h were required for a complete conversion from PbI_2 to $CH_3NH_3PbI_3$.[34] In vapor-crystallized method, on the contrary, the (001) peak of PbI_2 in the intermediate stage (30 min) disappeared at the final stage (60 min) of reaction. This

DOI: 10.1021/am508495r
ACS Appl. Mater. Interfaces 2015, 7, 3382−3388

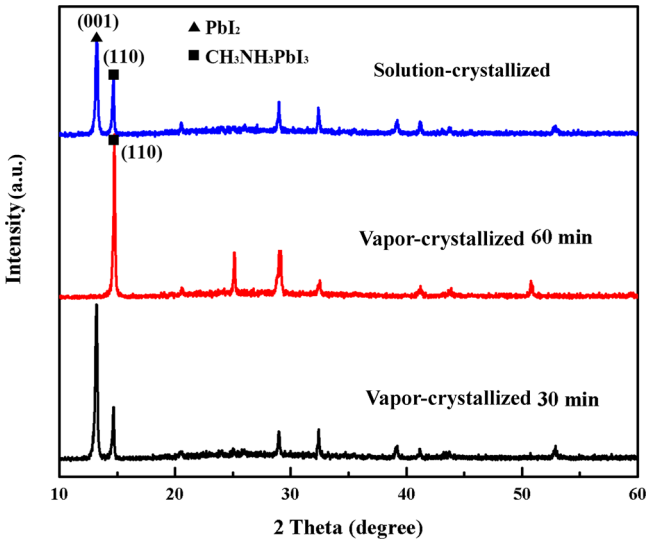

Figure 3. X-ray diffraction (XRD) patterns of vapor-crystallized perovskite at 30 and 60 min and solution-crystallized perovskite.

indicated that the insertion of CH_3NH_3I vapor into PbI_2 thin film was much more effective than that of CH_3NH_3I solution.

Spin-coating PbI_2 on flat surface usually led to large size of crystals. A complete conversion of PbI_2 to perovskite was difficult. Previous research suggested that confining the size of PbI_2 crystals within ~20−30 nm would significantly enhance the conversion rate.[8] But this is not possible for planar-structured cells. Therefore, vapor-crystallization would be an optimal method for two-step-deposited planar-structured solar cells to achieve full conversion of PbI_2 to $CH_3NH_3PbI_3$.

The morphology of perovskite was closely related to the optical and electrical properties of the devices, and thus was important for device performance enhancement. The ultraviolet−visible absorbance spectra for solution-crystallized and vapor-crystallized perovskite are shown in Figure 4. The absorption peaks showed no significant shift for the two categories of devices, but absorbance intensity for vapor-crystallized device was much higher than solution-crystallized device in the visible region (400−800 nm). Considering the same content of perovskite layer for both categories of devices, reduced absorption of solution-crystallized perovskite might not be assigned to band gap discrepancy. However, it could be due to the porous structure of solution-crystallized perovskite layer, which resulted in leakage of light.

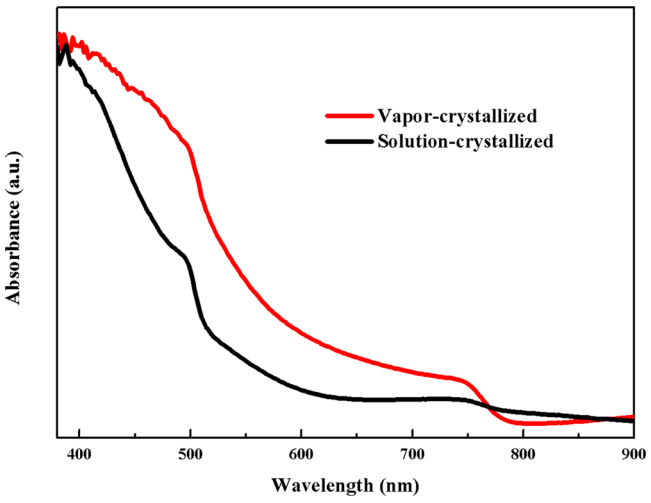

Figure 4. Ultraviolet−visible absorbance spectra of vapor-crystallized perovskite and solution-crystallized perovskite. The samples were prepared and tested on a flat glass.

To investigate the internal electronic structure of the two categories of devices, we presented a semilogarithmic plot of DC current responses under dark conditions in Figure 5. The

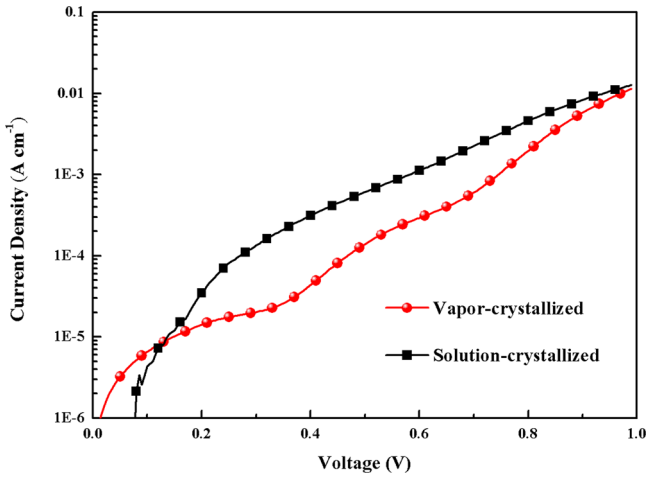

Figure 5. Semilogarithmic plot of dark current density of vapor-crystallized and solution-crystallized solar cells.

current response in middle forward bias region (300−700 mV), where the current density was governed by current flow through c-TiO_2, was analyzed using a single diode model and could be expressed as[35]

$$J(V) = J_s \exp\left(\frac{qV}{nkT} - 1\right) \quad (1)$$

where J is dark current, J_s is dark saturated current, q is electronic charge, V is applied bias, k is Boltzmann constant, T is temperature at the test condition, and n is the ideality factor describing the degree of deviation from idea diode model. The obtained dark $J-V$ characteristics in experiment were fitted in eq 1, which yielded $J_s = 9.89 \times 10^{-6}$ A/cm^2, $n = 2.4$ for vapor-crystallized device, and $J_s = 9.21 \times 10^{-5}$ A/cm^2, $n = 2.8$ for solution-crystallized device. The solution-crystallized devices showed almost ten-times the level of dark current and higher ideality factor compared to the vapor-crystallized device.

In a solar cell, charge carriers under dark condition moved in the opposite direction to that under illumination. The obtained net photocurrent density, J_{net}, in experiment could be expressed as,

$$J_{net} = J_{sc} - J_d \quad (2)$$

where J_{sc} is the short circuit current density, J_d is the dark current density. Suppressed dark current density was favorable for increasing photocurrent density. A major reason for increased dark current was additional carrier movement caused by recombination of charge carriers. Recombination of carries was associated with a joint effect of structural imperfections of the heterojunction, where electrons were captured by defeats, surface states or electron traps. Because we adopted the same blocking layer and HTM, the reduced recombination of charge carriers for vapor-crystallized devices could reasonably be attributed to its optimized morphology of perovskite layer.

DOI: 10.1021/am508495r
ACS Appl. Mater. Interfaces 2015, 7, 3382−3388

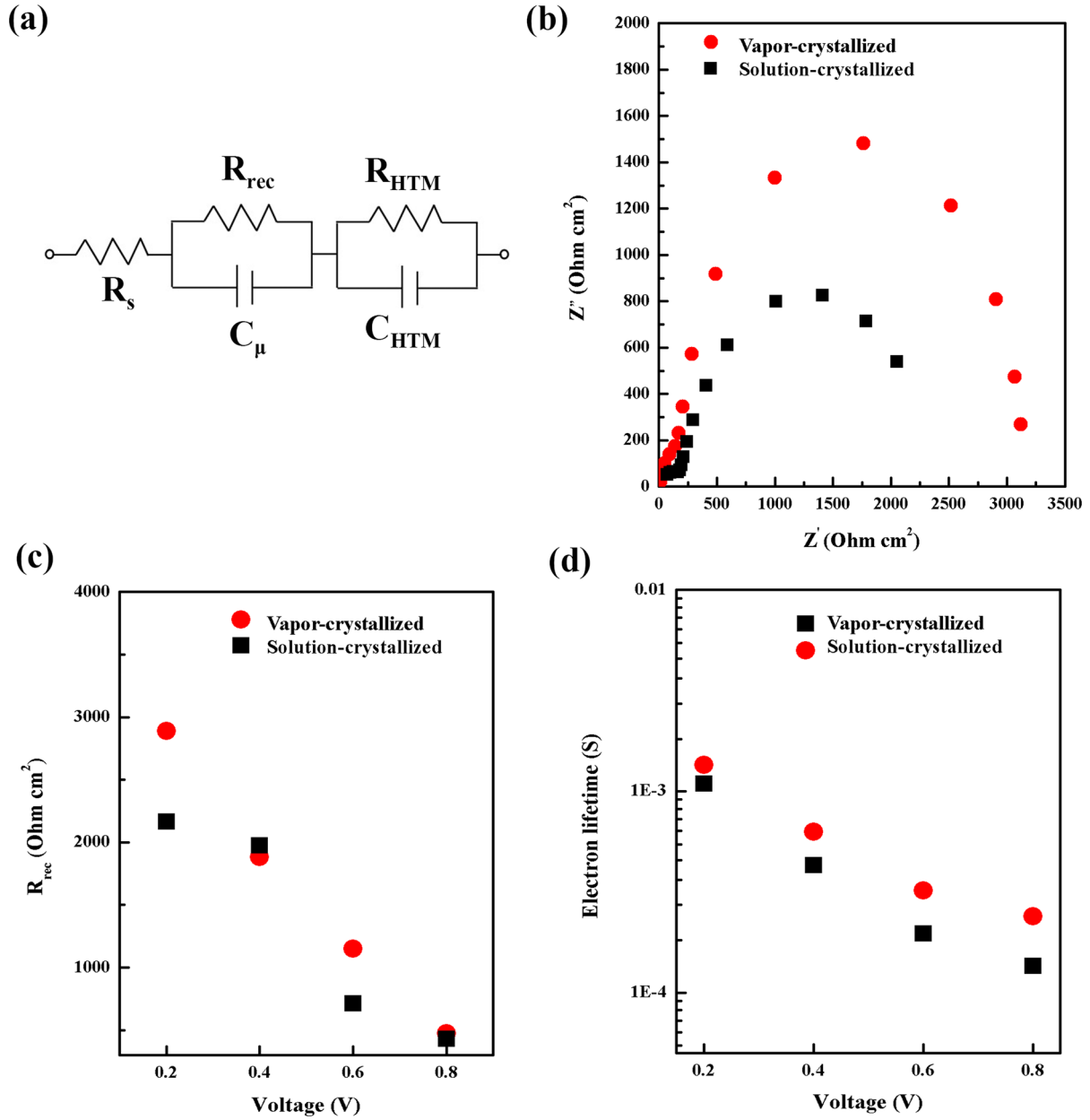

Figure 6. (a) Equivalent circuit employed for fitting, (b) electronic impedance spectroscopy at 200 mV of vapor-crystallized device and solution-crystallized device, (c) recombination resistance R_{rec}, and (d) electron lifetime τ_e for the two categories of devices.

To investigate the discrepancy of internal charge carrier transportation and recombination, we performed electronic impedance spectroscopy (EIS) from 1 Hz to 70k Hz under illuminated conditions,[36,37] and the obtained data were fitted by ZView software. The equivalent circuit for fitting shown in Figure 6a consisted of one series resistance R_s, one RC elements representing recombination resistance R_{rec} and a parallel chemical capacitance of perovskite film, and an additional RC elements for the interface between HTM and back contact.[38,39] Figure 6b presented representative Nyquist plot at 200 mV. For both devices, two clear arcs at high-frequency region and lower-frequency region were observed. The high-frequency arc was assigned to the process of hole transportation in Spiro-OMeTAD, and the lower one should originated from recombination resistance and chemical capacitance of perovskite film.

The calculated series resistance R_s for vapor-crystallized device was 12.9 Ω cm^2, much lower than that of solution-crystallized device of 58.5 Ω cm^2 and indicates lower loss for charge carrier transportation. This was possibly because vapor-crystallized perovskite demonstrated vertically oriented grains (see Figure 1d), which was favorable electron transportation through the perovskite layer.[9] The recombination resistance R_{rec}, reversely related to recombination rate and dependent on applied bias voltage, was plotted in Figure 6c.[40] The recombination rate was higher for solution-crystallized perovskite, revealed by higher level of R_{rec}.

Electron lifetime (τ_e) for two categories of devices was plotted in Figure 6d. Electron lifetime could be obtained from characteristic angle frequency of the peak in midfrequency region (f_{mid}) of the EIS Bode phase plot, and was calculated as $\tau_e = 1/(2\pi f_{mid})$.[41] The plot showed downward tendency with increased applied bias voltage, and we observed a generally

DOI: 10.1021/am508495r
ACS Appl. Mater. Interfaces 2015, 7, 3382−3388

higher electron lifetime for vapor-crystallized solar cells, which was in agreement of their higher recombination resistance compared with solution-crystallized devices.

Figure 7 showed the best-performing $J-V$ curves of two categories of solar cells under AM1.5 irradiation of 100w/cm^2.

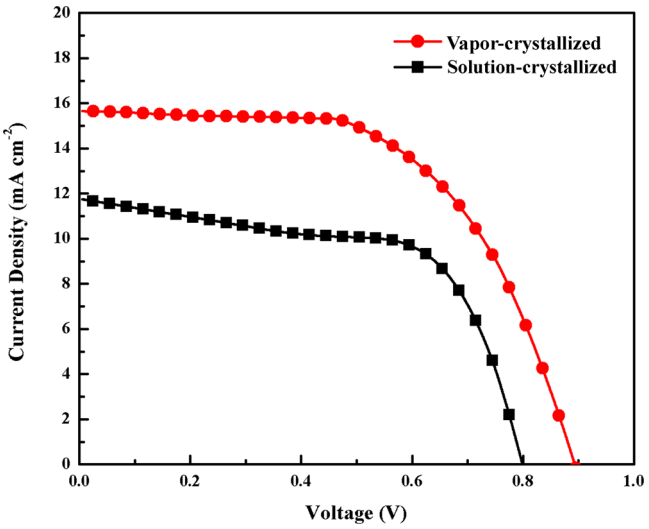

Figure 7. $J-V$ characteristics of best-performing vapor-crystallized and solution-crystallized solar cells under AM 1.5 irradiation of 100 mW/cm^2.

The solution-crystallized device demonstrated J_{sc} of 11.8 mA/cm^2, V_{oc} of 0.80 V and fill factor of 0.61 to yield power conversion efficiency (PCE) of 5.8%, while vapor-crystallized device showed J_{sc} = 15.7 mA/cm^2, V_{oc} = 0.89 V fill factor of 0.58 with a much higher PCE = 8.1%. The improved device efficiency was related to an overall effect of increased J_{sc} and V_{oc}. Higher J_{sc} for vapor-crystallized devices was associated a combined factor of light absorbance, charge transportation, recombination and charge collection. Vapor-crystallized devices demonstrated higher absorbance in visible region, which is shown in Figure 4, as well as lower recombination rate revealed by EIS measurement, which yielded more photogenerated electrons to be collected by anode. There was also a sound increase of open circuit voltage by 0.09 V. According to eq 1, V_{oc} could be obtained when dark current density equaled short current density

$$V_{oc} = \ln\left(\frac{J_{sc}}{J_s} + 1\right)nkT/q \quad (3)$$

Despite higher J_{sc}, the lower saturated dark current density J_s demonstrated by vapor-crystallized devices also created higher V_{oc}. The calculated results of V_{oc} were 0.787 V for solution-crystallized device and 0.885 V for vapor-crystallized device, which was in qualified agreement with measured data.

4. CONCLUSION

Comparing of vapor- and solution-crystallized methods, exposing PbI_2 to CH_3NH_3I vapor yielded compactly packed perovskite crystals, whereas dipping PbI_2 into CH_3NH_3I solution produced loosely aligned crystals. This indicated that moderate reaction of PbI_2 and CH_3NH_3I could result in optimized surface morphology of perovskite. As a result, vapor-crystallized devices showed enhanced absorption, suppressed dark current, lower recombination rate, and higher power conversion efficiency of vapor-crystallized devices, 8.1%, than the efficiency of solution-crystallized devices, 5.8%. Thus, it was concluded that the vapor-crystallized method was a much better method than the solution-crystallized method to obtain good photovoltaic performance for perovskite-based solar cells.

AUTHOR INFORMATION

Corresponding Author

*E-mail: wangninguestc@gmail.com. Tel & fax: (+86)28-83203807.

Notes

The authors declare no competing financial interest.

ACKNOWLEDGMENTS

This work was partially supported by China-Japan International Cooperation Program Funds (2010DFA61410 and 2011DFA50530), National Natural Science Foundations of China (51272035, 51272037, 51362026, and 51472043), National High Technology Research and Development Program of China (863 Program, 2011AA050522) and Program for New Century Excellent Talents in University (NCET-12-0097).

REFERENCES

(1) Kojima, A.; Teshima, K.; Shirai, Y.; Miyasaka, T. Organometal Halide Organometal Halide Perovskites as Visible-Light Sensitizers for Photovoltaic Cells. *J. Am. Chem. Soc.* **2009**, *131*, 6050−6051.

(2) Im, J.-H.; Lee, C.-R.; Lee, J.-W.; Park, S.-W.; Park, N.-G. 6.5% Efficient Perovskite Quantum-Dot-Sensitized Solar Cell. *Nanoscale* **2011**, *3*, 4088−4093.

(3) Kim, H.-S.; Lee, C.-R.; Im, J.-H.; Lee, K.-B.; Moehl, T.; Marchioro, A.; Moon, S.-J.; Humphry-Baker, R.; Yum, J.-H.; Moser, J. E.; Gratzel, M.; Park, N.-G. Lead Iodide Perovskite Sensitized All-Solid-State Submicron Thin Film Mesoscopic Solar Cell with Efficiency Exceeding 9%. *Sci. Rep.* **2012**, *2*, 591.

(4) Etgar, L.; Gao, P.; Xue, Z.; Peng, Q.; Chandiran, A. K.; Liu, B.; Nazeeruddin, M. K.; Grätzel, M. Mesoscopic $CH_3NH_3PbI_3/TiO_2$ Heterojunction Solar Cells. *J. Am. Chem. Soc.* **2012**, *134*, 17396−17399.

(5) Heo, J. H.; Im, S. H.; Noh, J. H.; Mandal, T. N.; Lim, C.-S.; Chang, J. A.; Lee, Y. H.; Kim, H.-j.; Sarkar, A.; NazeeruddinMd, K.; Gratzel, M.; Seok, S. I. Efficient Inorganic-Organic Hybrid Heterojunction Solar Cells Containing Perovskite Compound and Polymeric Hole Conductors. *Nat. Photon* **2013**, *7*, 486−491.

(6) Lee, M. M.; Teuscher, J.; Miyasaka, T.; Murakami, T. N.; Snaith, H. J. Efficient Hybrid Solar Cells Based on Meso-Superstructured Organometal Halide Perovskites. *Science* **2012**, *338*, 643−647.

(7) Ball, J. M.; Lee, M. M.; Hey, A.; Snaith, H. J. Low-temperature Processed Meso-Superstructured to Thin-Film Perovskite Solar Cells. *Energy Environ. Sci.* **2013**, *6*, 1739−1743.

(8) Burschka, J.; Pellet, N.; Moon, S.-J.; Humphry-Baker, R.; Gao, P.; Nazeeruddin, M. K.; Gratzel, M. Sequential Deposition as A Route to High-Performance Perovskite-Sensitized Solar Cells. *Nature* **2013**, *499*, 316−319.

(9) Aharon, S.; Cohen, B. E.; Etgar, L. Hybrid Lead Halide Iodide and Lead Halide Bromide in Efficient Hole Conductor Free Perovskite Solar Cell. *J. Phys. Chem. C* **2014**, *118*, 17160−17165.

(10) Park, N.-G. Organometal Perovskite Light Absorbers Toward a 20% Efficiency Low-Cost Solid-State Mesoscopic Solar Cell. *J. Phys. Chem. Lett.* **2013**, *4*, 2423−2429.

(11) Kim, H.-S.; Im, S. H.; Park, N.-G. Organolead Halide Perovskite: New Horizons in Solar Cell Research. *J. Phys. Chem. C* **2014**, *118*, 5615−5625.

(12) Leijtens, T.; Lauber, B.; Eperon, G. E.; Stranks, S. D.; Snaith, H. J. Importance of Perovskite Pore Filling in Organometal Mixed Halide

DOI: 10.1021/am508495r
ACS Appl. Mater. Interfaces 2015, 7, 3382−3388

Sensitized TiO_2-Based Solar Cells. *J. Phys. Chem. Lett.* **2014**, *5*, 1096−1102.
(13) Bach, U.; Lupo, D.; Comte, P.; Moser, J. E.; Weissortel, F.; Salbeck, J.; Spreitzer, H.; Gratzel, M. Solid-State Dye-Sensitized Mesoporous TiO_2 Solar Cells with High Photon-to-Electron Conversion Efficiencies. *Nature* **1998**, *395*, 583−585.
(14) Abate, A.; Saliba, M.; Hollman, D. J.; Stranks, S. D.; Wojciechowski, K.; Avolio, R.; Grancini, G.; Petrozza, A.; Snaith, H. J. Supramolecular Halogen Bond Passivation of Organic−Inorganic Halide Perovskite Solar Cells. *Nano Lett.* **2014**, *14*, 3247−3254.
(15) Saliba, M.; Tan, K. W.; Sai, H.; Moore, D. T.; Scott, T.; Zhang, W.; Estroff, L. A.; Wiesner, U.; Snaith, H. J. Influence of Thermal Processing Protocol upon the Crystallization and Photovoltaic Performance of Organic−Inorganic Lead Trihalide Perovskites. *J. Phys. Chem. C* **2014**, *118*, 17171−17177.
(16) Liu, M.; Johnston, M. B.; Snaith, H. J. Efficient Planar Heterojunction Perovskite Solar Cells by Vapour Deposition. *Nature* **2013**, *501*, 395−398.
(17) Docampo, P.; Ball, J. M.; Darwich, M.; Eperon, G. E.; Snaith, H. J. Efficient Organometal Trihalide Perovskite Planar-Heterojunction Solar Cells on Flexible Polymer Substrates. *Nat. Commun.* **2013**, *4*.
(18) Hanusch, F. C.; Wiesenmayer, E.; Mankel, E.; Binek, A.; Angloher, P.; Fraunhofer, C.; Giesbrecht, N.; Feckl, J. M.; Jaegermann, W.; Johrendt, D.; Bein, T.; Docampo, P. Efficient Planar Heterojunction Perovskite Solar Cells Based on Formamidinium Lead Bromide. *J. Phys. Chem. Lett.* **2014**, *5*, 2791−2795.
(19) Liu, D. Y.; Kelly, T. L. Perovskite Solar Cells with a Planar Heterojunction Structure Prepared Using Room-Temperature Solution Processing Techniques. *Nat. Photonics* **2014**, *8*, 133−138.
(20) Liang, P. W.; Liao, C. Y.; Chueh, C. C.; Zuo, F.; Williams, S. T.; Xin, X. K.; Lin, J. J.; Jen, A. K. Y. Additive Enhanced Crystallization of Solution-Processed Perovskite for Highly Efficient Planar-Heterojunction Solar Cells. *Adv. Mater.* **2014**, *26*, 3748−3754.
(21) Liang, L.; Huang, Z.; Cai, L.; Chen, W.; Wang, B.; Chen, K.; Bai, H.; Tian, Q.; Fan, B. Magnetron Sputtered Zinc Oxide Nanorods as Thickness-Insensitive Cathode Interlayer for Perovskite Planar-Heterojunction Solar Cells. *ACS Appl. Mater. Interface* **2014**, *6*, 20585−20589.
(22) Eperon, G. E.; Burlakov, V. M.; Goriely, A.; Snaith, H. J. Neutral Color Semitransparent Microstructured Perovskite Solar Cells. *ACS Nano* **2013**, *8*, 591−598.
(23) Eperon, G. E.; Stranks, S. D.; Menelaou, C.; Johnston, M. B.; Herz, L. M.; Snaith, H. J. Formamidinium Lead Trihalide: A Broadly Tunable Perovskite for Efficient Planar Heterojunction Solar Cells. *Energy Environ. Sci.* **2014**, *7*, 982−988.
(24) Zhang, F.; Yang, X.; Wang, H.; Cheng, M.; Zhao, J.; Sun, L. Structure Engineering of Hole−Conductor Free Perovskite-Based Solar Cells with Low-Temperature-Processed Commercial Carbon Paste As Cathode. *ACS Appl. Mater. Interface* **2014**, *6*, 16140−16146.
(25) Eperon, G. E.; Burlakov, V. M.; Docampo, P.; Goriely, A.; Snaith, H. J. Morphological Control for High Performance, Solution-Processed Planar Heterojunction Perovskite Solar Cells. *Adv. Funct. Mater.* **2014**, *24*, 151−157.
(26) Bi, D.; El-Zohry, A. M.; Hagfeldt, A.; Boschloo, G. Improved Morphology Control Using a Modified Two-Step Method for Efficient Perovskite Solar Cells. *ACS Appl. Mater. Interface* **2014**, *6*, 18751−18757.
(27) Ke, W.; Fang, G.; Wang, J.; Qin, P.; Tao, H.; Lei, H.; Liu, Q.; Dai, X.; Zhao, X. Perovskite Solar Cell with An Efficient TiO_2 Compact Film. *ACS Appl. Mater. Interface* **2014**, *6*, 15959−15965.
(28) Wang, K.-C.; Shen, P.-S.; Li, M.-H.; Chen, S.; Lin, M.-W.; Chen, P.; Guo, T.-F. Low-Temperature Sputtered Nickel Oxide Compact Thin Film as Effective Electron Blocking Layer for Mesoscopic NiO/$CH_3NH_3PbI_3$ Perovskite Heterojunction Solar Cells. *ACS Appl. Mater. Interface* **2014**, *6*, 11851−11858.
(29) Chen, Q.; Zhou, H. P.; Hong, Z. R.; Luo, S.; Duan, H. S.; Wang, H. H.; Liu, Y. S.; Li, G.; Yang, Y. Planar Heterojunction Perovskite Solar Cells via Vapor-Assisted Solution Process. *J. Am. Chem. Soc.* **2014**, *136*, 622−625.
(30) Chen, C.-W.; Kang, H.-W.; Hsiao, S.-Y.; Yang, P.-F.; Chiang, K.-M.; Lin, H.-W. Efficient and Uniform Planar-Type Perovskite Solar Cells by Simple Sequential Vacuum Deposition. *Adv. Mater.* **2014**, *26*, 6647−6652.
(31) Chen, C.-W.; Hsiao, S.-Y.; Chen, C.-Y.; Kang, H.-W.; Huang, Z.-Y.; Lin, H.-W. Optical properties of organometal halide perovskite thin films and general device structure design rules for perovskite single and tandem solar cells. *J. Mater. Chem. A* **2015**.
(32) Beckmann, P. A. Correction: A Review of Polytypism in Lead Iodide. *Cryst. Res. Technol.* **2010**, *45*, 455−460.
(33) Baikie, T.; Fang, Y.; Kadro, J. M.; Schreyer, M.; Wei, F.; Mhaisalkar, S. G.; Graetzel, M.; White, T. J. Synthesis and Crystal Chemistry of the Hybrid Perovskite $(CH_3NH_3)PbI_3$ for Solid-State Sensitised Solar Cell Applications. *J. Mater. Chem. A* **2013**, *1*, 5628−5641.
(34) Liang, K.; Mitzi, D. B.; Prikas, M. T. Synthesis and Characterization of Organic−Inorganic Perovskite Thin Films Prepared Using a Versatile Two-Step Dipping Technique. *Chem. Mater.* **1998**, *10*, 403−411.
(35) Shanmugam, M.; Durcan, C. A.; Jacobs-Gedrim, R.; Yu, B. Layered Semiconductor Tungsten Disulfide: Photoactive Material in Bulk Heterojunction Solar Cells. *Nano Energy* **2013**, *2*, 419−424.
(36) Wang, Q.; Moser, J.-E.; Grätzel, M. Electrochemical Impedance Spectroscopic Analysis of Dye-Sensitized Solar Cells. *J. Phys. Chem. B* **2005**, *109*, 14945−14953.
(37) Dualeh, A.; Moehl, T.; Tétreault, N.; Teuscher, J.; Gao, P.; Nazeeruddin, M. K.; Grätzel, M. Impedance Spectroscopic Analysis of Lead Iodide Perovskite-Sensitized Solid-State Solar Cells. *ACS Nano* **2013**, *8*, 362−373.
(38) Yella, A.; Heiniger, L.-P.; Gao, P.; Nazeeruddin, M. K.; Grätzel, M. Nanocrystalline Rutile Electron Extraction Layer Enables Low-Temperature Solution Processed Perovskite Photovoltaics with 13.7% Efficiency. *Nano Lett.* **2014**, *14*, 2591−2596.
(39) Fabregat-Santiago, F.; Bisquert, J.; Palomares, E.; Haque, S. A.; Durrant, J. R. Impedance spectroscopy study of dye-sensitized solar cells with undoped spiro-OMeTAD as hole conductor. *J. Appl. Phys.* **2006**, *100*, 034510.
(40) Christians, J. A.; Fung, R. C. M.; Kamat, P. V. An Inorganic Hole Conductor for Organo-Lead Halide Perovskite Solar Cells. Improved Hole Conductivity with Copper Iodide. *J. Am. Chem. Soc.* **2013**, *136*, 758−764.
(41) Bisquert, J.; Fabregat-Santiago, F.; Mora-Seró, I.; Garcia-Belmonte, G.; Giménez, S. Electron Lifetime in Dye-Sensitized Solar Cells: Theory and Interpretation of Measurements. *J. Phys. Chem. C* **2009**, *113*, 17278−17290.

DOI: 10.1021/am508495r
ACS Appl. Mater. Interfaces 2015, 7, 3382−3388